Article

Influence of Sputtering Temperature of TiO$_2$ Deposited onto Reduced Graphene Oxide Nanosheet as Efficient Photoanodes in Dye-Sensitized Solar Cells

Foo Wah Low [1,2,*] , **Goh Chin Hock** [2,*] , **Muhammad Kashif** [3] , **Nurul Asma Samsudin** [2] ,
Chien Fat Chau [4,*] , **Amaliyah Rohsari Indah Utami** [5] , **Mohammad Aminul Islam** [2,6] ,
Cheng Yong Heah [7,8] , **Yun Ming Liew** [8] , **Chin Wei Lai** [9] , **Nowshad Amin** [2] and
Sieh Kiong Tiong [2]

[1]   Department of Electrical & Electronic Engineering, Lee Kong Chian Faculty of Engineering & Science,
      Universiti Tunku Abdul Rahman, Bandar Sungai Long, Kajang 43000, Selangor, Malaysia
[2]   Institute of Sustainable Energy, Universiti Tenaga Nasional (The Energy University), Jalan IKRAM-UNITEN,
      Kajang 43000, Selangor, Malaysia; nurul.asma@uniten.edu.my (N.A.S.); aminbgm@gmail.com (M.A.I.);
      nowshad@uniten.edu.my (N.A.); siehkiong@uniten.edu.my (S.K.T.)
[3]   School of Electrical & Information Engineering, Tianjin University, 92 Weijin Road, Nankai District,
      Tianjin 300072, China; kashiff.farooq@gmail.com
[4]   College of Engineering, Universiti Tenaga Nasional (The Energy University), Jalan IKRAM-UNITEN,
      Kajang 43000, Selangor, Malaysia
[5]   Engineering Physics, School of Electrical Engineering, Telkom University, Bandung 40257, Indonesia;
      amaliyahriu@telkomuniversity.ac.id
[6]   Department of Electrical Engineering, University of Malaya, Jalan Universiti,
      Kuala Lumpur 50603, Selangor, Malaysia
[7]   Faculty of Engineering Technology, Universiti Malaysia Perlis (UniMAP), Sungai Chuchuh, Padang Besar,
      Kangar 02100, Perlis, Malaysia; cyheah@unimap.edu.my
[8]   Center of Excellence Geopolymer and Green Technology (CeGeoGTech), School of Materials Engineering,
      Universiti Malaysia Perlis (UniMAP), Kangar 01000, Perlis, Malaysia; ymliew@unimap.edu.my
[9]   Nanotechnology and Catalysis Research Centre (NANOCAT), Level 3, Block A,
      Institute for Advanced Studies (IAS), University of Malaya (UM), Kuala Lumpur 50603, Selangor, Malaysia;
      cwlai@um.edu.my
*   Correspondence: lowfw@utar.edu.my or raymondlow85@gmail.com (F.W.L.);
      chinhock@uniten.edu.my (G.C.H.); cchienfat@uniten.edu.my (C.F.C.)

check for
updates

Abstract: Renewable solar energy is the key target to reduce fossil fuel consumption, minimize global warming issues, and indirectly minimizes erratic weather patterns. Herein, the authors synthesized an ultrathin reduced graphene oxide (rGO) nanosheet with ~47 nm via an improved Hummer's method. The TiO$_2$ was deposited by RF sputtering onto an rGO nanosheet with a variation of temperature to enhance the photogenerated electron or charge carrier mobility transport for the photoanode component. The morphology, topologies, element composition, crystallinity as well as dye-sensitized solar cells' (DSSCs) performance were determined accordingly. Based on the results, FTIR spectra revealed presence of Ti-O-C bonds in every rGO-TiO$_2$ nanocomposite samples at 800 cm^{-1}. Besides, XRD revealed that a broad peak of anatase TiO$_2$ was detected at ~25.4° after incorporation with the rGO. Furthermore, it was discovered that sputtering temperature of 120 °C created a desired power conversion energy (PCE) of 7.27% based on the *J-V* plot. Further increase of the sputtering temperature to 160 °C and 200 °C led to excessive TiO$_2$ growth on the rGO nanosheet, thus resulting in undesirable charge recombination formed at the photoanode in the DSSC device.

1. Introduction

The demand of global energy usage has increased tremendously by 0.9%, equivalent to a 120 million tonnes of oil (Mtoe) in 2019 as compared to 2018 [1]. The consumption of fossil fuel (i.e., oil, coal, gas) is expected to keep rising due to economic growth and increasing population around the world. Further emission of fossil fuels produces carbon monoxide (CO) gas, a driver of the greenhouse effect. This continuous reliance on conventional energy resources will lead to a negative impact on the global warming crisis [2]. These climate change issues will result in erratic patterns like ice melt, sea levels and ocean acidification, plants and animals, and also social effects [3].

In this context, transitioning away from fossil fuels by executing alternative research for renewable energy with low-carbon sources is mandatory. Solar energy is an obvious choice towards a clean energy source, which is free, abundant, and everlasting source that could be provided in a pollution free manner. Nowadays, photovoltaic (PV) technologies have received great attention from researchers due to its ability in generating electricity that is clean, inexpensive, and sustainable, from sunlight [4–6]. To date, these technologies are achievable for the optimization of crystalline silicon solar cells at a power conversion energy (PCE) of about 27.6% [7]. Further generation in thin film solar cells involving CIGS, CdTe, and amorphous silicon, could achieve as high as 23.4% in 2019 [7–9]. However, these technologies have high cost production and mass scale panels [10].

Emerging PV technology cells of dye-sensitized solar cells (DSSCs), relatively low-cost, and ease for fabrication, have obtained an ideal PCE of 12.6% [11]. Practically, the PCE performance of DSSCs usually depends on the materials used in the photoanode part. Thus, the photoanode is the crucial element, which is applicable for absorbing the incoming light and allowing it to pass into the dyes for photoelectrochemical process [12]. Commonly, titanium dioxide (TiO$_2$) is utilized for photoanodes due to its high thin film transparency and good photocatalytic characteristics [13,14]. However, TiO$_2$ has some drawbacks such as recombination and the potential of causing undesirable effects for the excited photogenerated electrons in the interfacial transfer and leads to low PCE performance [15].

Recently, a two-dimensional (2D) carbon nanomaterial, graphene, has attracted interest with several outstanding properties that fit the DSSCs and its mechanism features in photoanode [16–18]. Furthermore, graphene exhibits efficient charge carrier transport, which will probably facilitate the excited electrons' flow towards the outer circuit and improve the overall PCE performance of DSSCs [19]. Moreover, graphene has excellent optical transparency properties with good absorption rate that could efficiently allow the illumination light into the dye molecules. However, graphene without functionalized or further incorporation with other metal oxide is insufficient to be applied as a photoanode [20]. Besides, it also suffers from lattice defects and this leads to low PCE for DSSCs [21].

Researchers have attempted to improve the PCE performance of DSSCs by incorporating the TiO$_2$ with reduced graphene oxide (rGO) as reported elsewhere [22,23]. Recently, it has been discovered that hydrothermal deposition of rGO could be deposited onto TiO$_2$ with various concentrations of GO for photocatalytic degradation of RhB dye [24]. Later, Sayali et al. and their group found that the rGO-TiO$_2$ nanocomposite preparation via ultrasound assisted/sonochemical method could obtain good Ti-O-C bonding [25]. Some recent updates about rGO-TiO$_2$ formation via different techniques are shown in Table 1. However, these techniques are emphasized on surface deposition/coating and there is a lack of accurate bonding onto the material lattice and inadequate concentration formation by the dopant.

In this paper, the preparation rGO-TiO$_2$ nanocomposite as photoanode for DSSCs is reported via an RF sputtering technique approach. Specifically, an optimization of sputtering temperature of the TiO$_2$ target and direct penetration of the rGO nanosheet could suppress the recombination

while improving the photoinduced charge carrier transport. Furthermore, the sputtering technique is promising to maximize the opportunity to fill the oxygen vacancy to reduce the intrinsic defect of rGO in oxides lattice with TiO_2. Herein, RF sputtering is a better approach comparable to other physical coating or depositing for exterior dopants. In fact, this technique is associated with a better adhesion and uniform distribution onto rGO nanosheet with efficient atom bombardment. Until now, detailed studies of rGO decorated with TiO_2 with various sputtering temperatures onto rGO nanosheet for DSSCs performance are still lacking. Yet, the influence of sputtering temperature of TiO_2 onto rGO nanosheet, reaction mechanism, and their physical/chemical characteristics as photoanode remains unclear. Henceforth, comprehensive work is conducted to optimize the rGO-TiO_2 nanocomposite as photoanode element for DSSCs and to be tested under 100 W solar illumination power.

Table 1. Summary of rGO-TiO_2 nanocomposites by different techniques.

Composite Formation	Optimized Concentration	Dopants	Method	Findings	Ref.
rGO/TiO_2	3 wt%	GO	solvothermal	ACT degradation and mineralization on photocatalytic	[26]
TiO_2-rGO	0.5 wt%	GO	hydrothermal	FM photodegradation	[27]
TiO_2-rGO	0.4 wt%	GO	hydrothermal	DSSCs	[28]
rGO-TiO_2	0.5mg	rGO	hydrothermal	DSSCs	[29]
Ag/rGO/TiO_2	-	GO	solvothermal	Plasmonic DSSCs	[30]

2. Experimental Details

2.1. Materials

Graphite powder (<20 μm; 99.99%); potassium permanganate, $KMnO_4$ (≥99.0%); hydrazine solution (35 wt% in H_2O); fluorine doped tin oxide coated glass slide, FTO coated glass (surface resistivity: ~7 Ω/sq), Di-tetrabutylammonium cis-bis(isothiocyanato)bis(2,2′-bipyridyl-4,4′-dicarboxylato)ruthenium(II) (ruthenium dye), platinum, Pt (≥99.9% trace metals basis), and silver conductive paste were purchased from Sigma Aldrich, Malaysia. Sulfuric acid, H_2SO_4 (95–97%); ortho-phosphoric acid, H_3PO_4 (85%); hydrogen peroxide, H_2O_2 (30%); hydrochloric acid fuming, HCl (37.0%); absolute ethanol, C_2H_5OH (≥99.5%), acetonitrile, C_2H_3N (41.05 g/mol), and potassium iodide electrolyte, KI (≥99.0%) were purchased from Merck, Malaysia. Titanium target for sputtering (99.99% purity, diameter in 50,800 μm with thickness of 6350 μm) was purchased from ULVAC Inc. The deposition process of TiO_2 onto rGO nanosheet was conducted using an RF sputtering machine at SIRIM Berhad, Malaysia.

2.2. GO and rGO Preparation

Ideal GO and rGO nanosheets were synthesized via improved Hummer's method and chemical reduction technique as reported in our previous work [31–33]. The overall reaction is illustrated in Figure 1a whereas the chemical structure of graphite, GO, and rGO are shown in Figure 1b–d, respectively. Comprehensively, GO was prepared from graphite powder as the precursor material via improved Hummer's method. A total of 1.5 g of graphite powder was poured into an acid ratio of 9:1 (H_2SO_4:H_3PO_4) [34]. Next, 9.0 g of oxidizing agent, $KMnO_4$, was then slowly poured into the mixture under ice bath condition (<20 °C). The solvent color changed from dark purplish green to dark brown, indicating that the oxidizing process was taking place. After 24 h, the solvent mixture was slowly transferred into ~200 mL ice solution and the overall reaction was conducted under ice bath condition. The oxidization process was terminated by adding 3 mL of H_2O_2 dropwise into the mixture and turned the color from dark brown to light brownish, indicating that a high oxidation level of graphite was well formed [34]. The suspension was centrifuged and washed with diluted HCl and DI water until pH7 was achieved. The sol-gel GO byproduct was formed after being dried for 24 h in a dry oven. Furthermore, 1.26 g of fine GO was produced from graphite powder. For rGO synthesis, it was well prepared via a chemically reduction process. Additionally, 300 mg of GO flakes were

added into 100 mL distilled water while 100 μL of hydrazine solvent was immediately dropped into the mixture. The overall reaction was heated under oil bath conditions and maintained at ~80 °C [35]. The mixture was centrifuged and the supernatant was decanted away. Lastly, approximately 0.84 g of rGO samples were formed after being dried in a dry oven for 24 h. Henceforth, the yield production of synthesized rGO from GO went up to 67%.
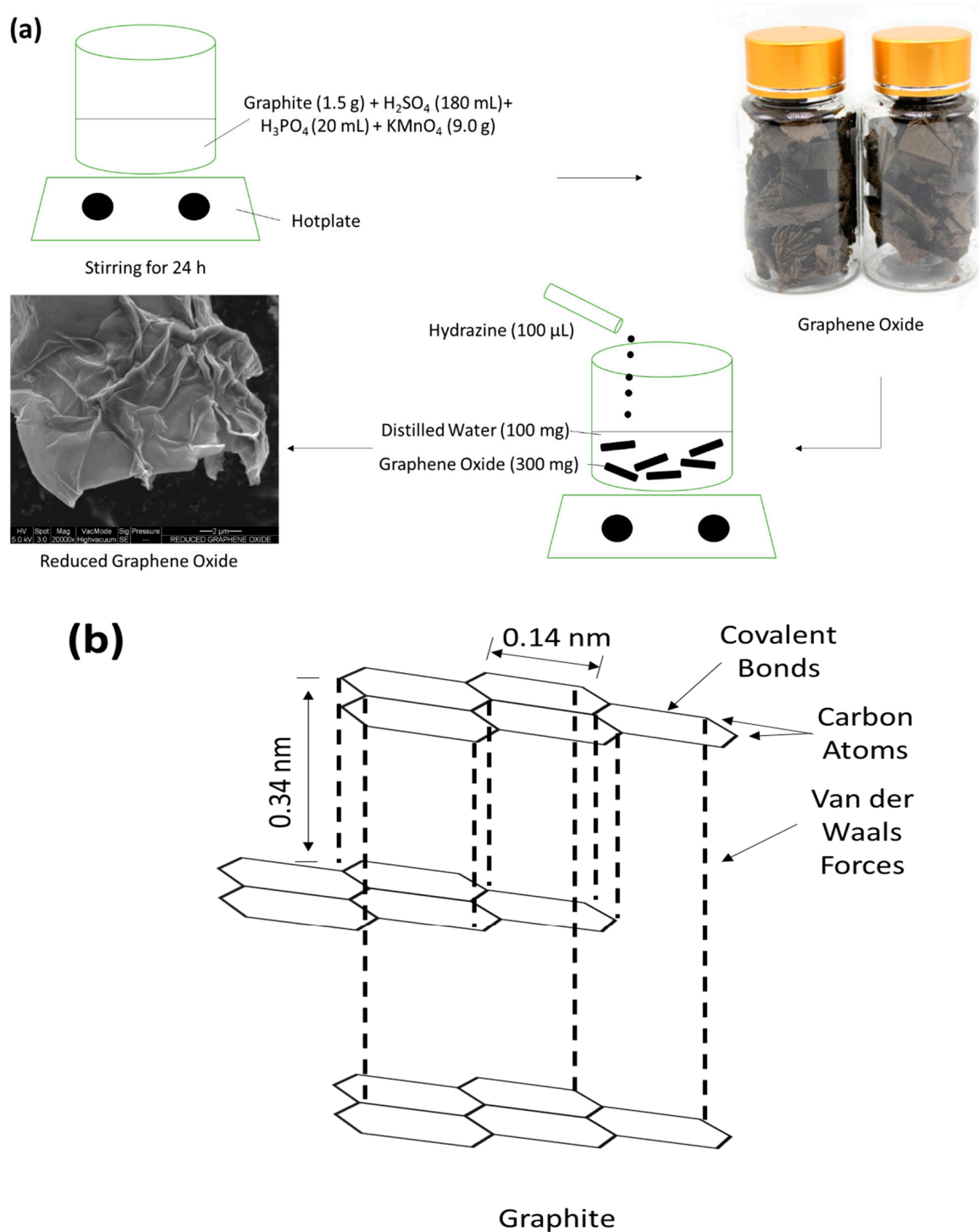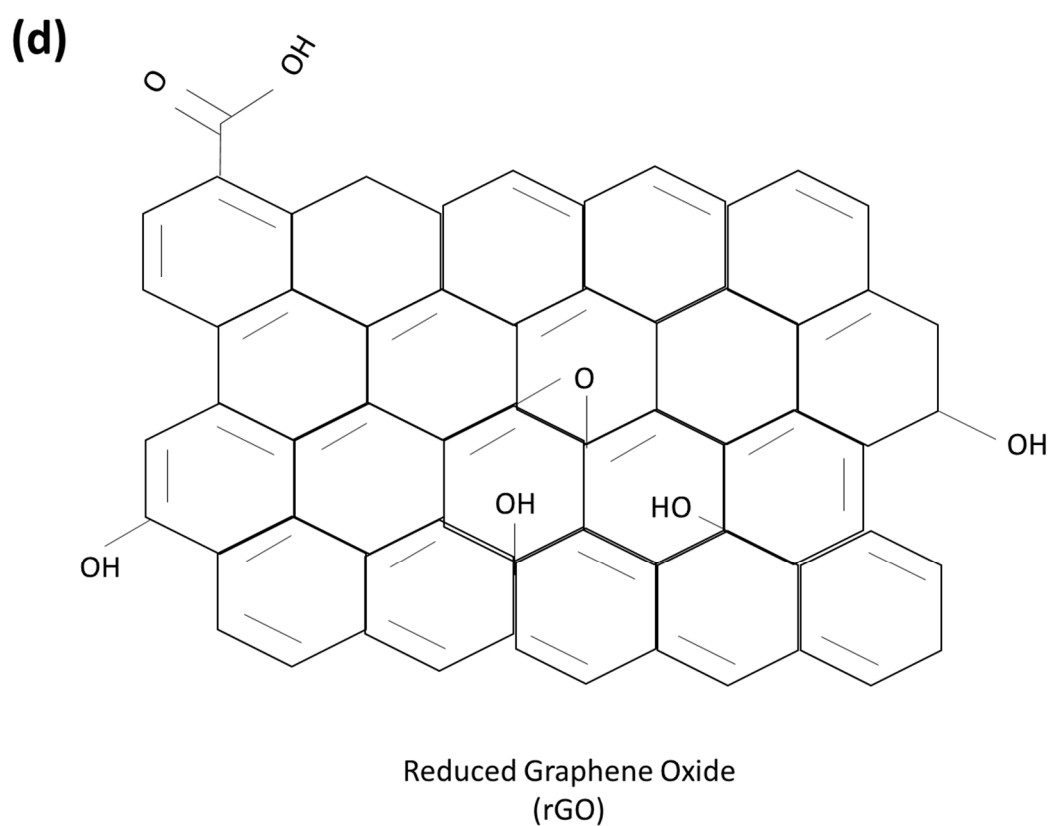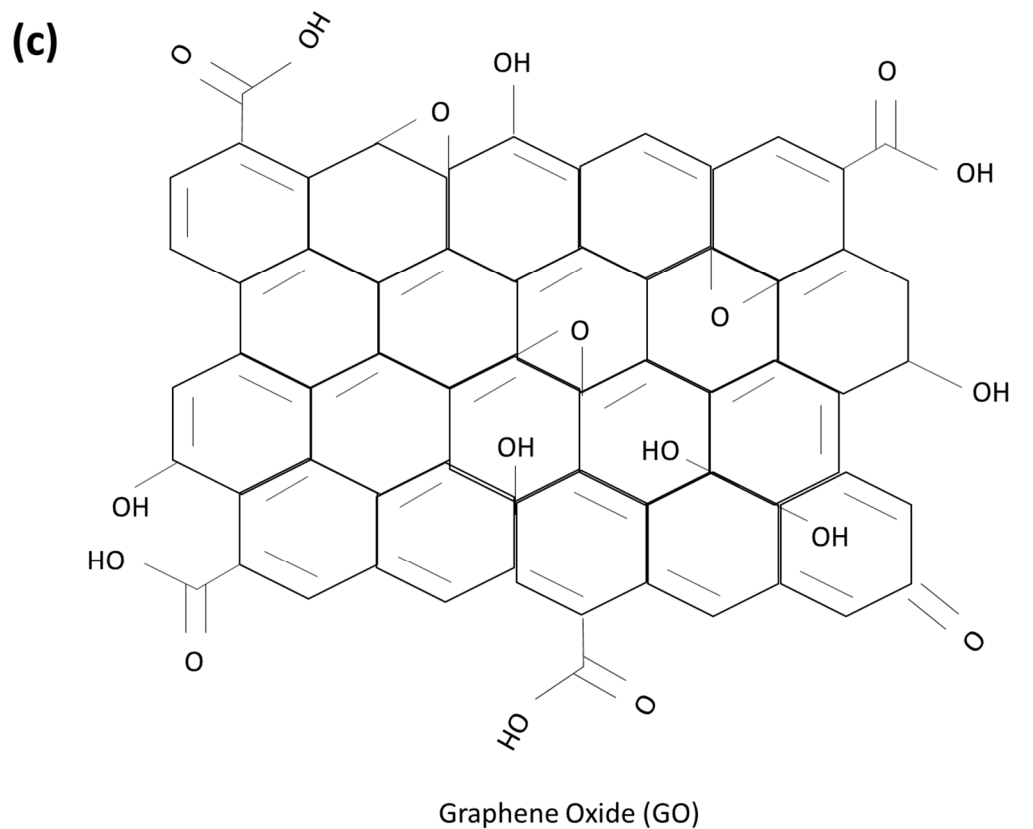

(a)

Graphite (1.5 g) + H_2SO_4 (180 mL)+ H_3PO_4 (20 mL) + $KMnO_4$ (9.0 g)

Hotplate

Stirring for 24 h

Graphene Oxide

Hydrazine (100 μL)

Distilled Water (100 mg)
Graphene Oxide (300 mg)

Reduced Graphene Oxide

(b)

0.14 nm

Covalent Bonds

Carbon Atoms

Van der Waals Forces

0.34 nm

Graphite

Figure 1. *Cont.*

(c)

Graphene Oxide (GO)

(d)

Reduced Graphene Oxide
(rGO)

Figure 1. (**a**) Schematic diagram of GO and rGO synthesis, chemical structure of (**b**) graphite, (**c**) GO, and (**d**) rGO.

2.3. rGO-TiO$_2$ Nanocomposite Formation

The rGO-TiO$_2$ nanocomposite via sputtering technique was prepared as an efficient photoanode for DSSCs devices as depicted in Figure 2. Firstly, the rGO nanosheet layer was deposited onto FTO glass via an electrodeposition technique as reported in our finding [33]. Size of the entire DSSCs device had been fixed with 2 cm × 2 cm area for both the anode and the cathode. The rGO was deposited on FTO glass for the anode part with an active area of 0.67 cm^2. From our understanding, the sputtering method is one of the effective routes to produce photoanode to achieve an ideal PCE of DSSC performance [36]. In other words, the sputtering technique has the potential to allow more dopant atom particles to penetrate onto the rGO nanosheet under high acceleration and are well formed within a second [37]. Thus, it would enhance the properties of rGO-TiO$_2$ nanocomposites in terms of charge carrier transport rate, resulting in high PCE of DSSC performance. In this typical procedure, several FTO with coated rGO were placed for RF sputtering with different sputtering temperatures of 40, 80, 120, 160, and 200 °C. The utilized titanium dioxide target was placed in a chamber with the optimization of being placed with distance of 10 cm apart [33]. For the uniformity of dopant onto the rGO nanosheet, the sputtering duration of TiO$_2$ and input power were maintained at 60 s and 150 W, respectively. The flow rate of Argon, Ar, gas was 15 mL/min, pressure at 266.64 mPa with base pressure of 0.67 mPa. Finally, the rGO-TiO$_2$ nanocomposite was successfully formed for the photoanode element.
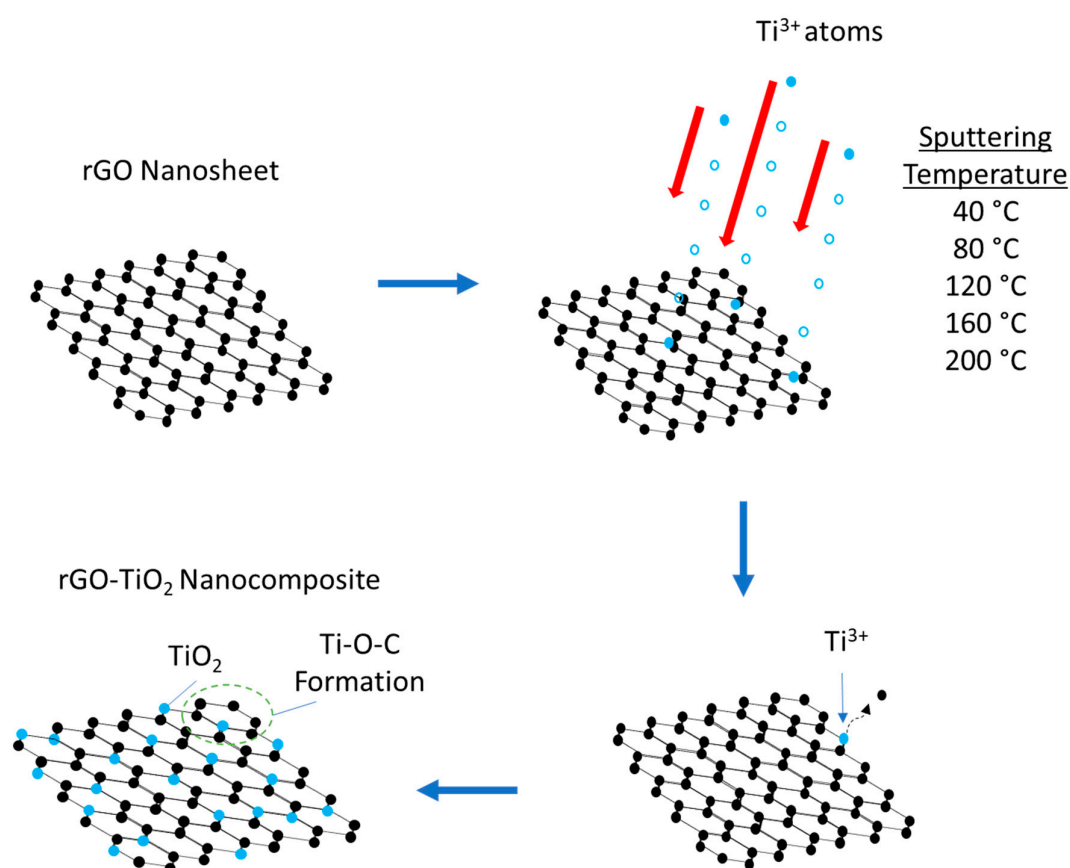

Figure 2. Sputtering mechanism process of rGO-TiO$_2$ nanocomposite.

2.4. DSSCs Fabrication

Theoretically, a working DSSCs device is integrated in a sandwich configuration, which consists of TCO/photoanodes/dye/electrolyte/counter electrode/TCO as shown in Figure 3. Practically, our study aims at modification of rGO photoanodes (conventional in TiO$_2$ material), which is the core element for the incoming light absorption ability. The main role of the photoanode is used to allow the excited

photo-electron from dye molecules into the conduction band of TiO$_2$ under the illumination process. In addition, the incorporation of rGO with TiO$_2$ is applied to lift-down the incoming electrons at TiO$_2$ since it is a wide band gap metal oxide semiconductor material (3.2 eV). The role of rGO also helps in the internal movement of exciton electrons from the valence band of TiO$_2$ into the conduction band of TiO$_2$, where it is possesses high carrier mobility with almost zero band gap characteristics [16]. In this way, the rGO-TiO$_2$ nanocomposite could efficiently transfer the excited photo-electrons by minimizing the charge recombination.
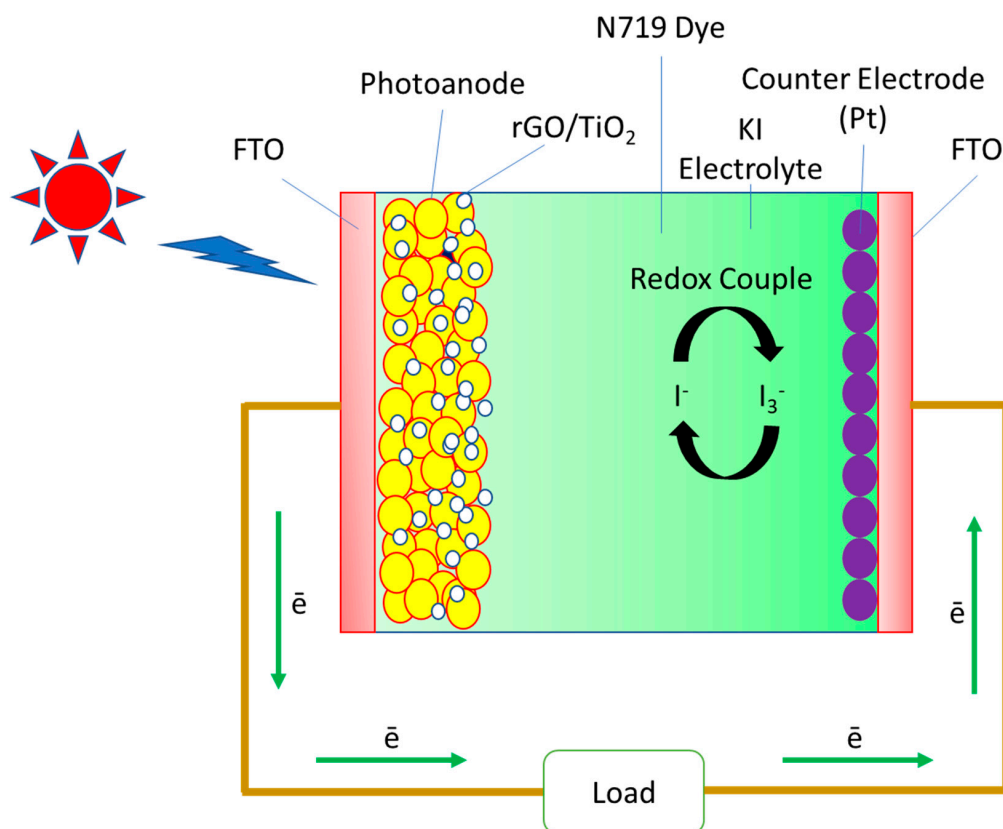
Figure 3. DSSCs schematic diagram of rGO-TiO$_2$ nanocomposite photoanode.

For details of DSSCs fabrication process, photoanode contained rGO-TiO$_2$ was soaked into a solvent containing 0.5 mL N719 dye (0.3 mM) and C$_2$H$_5$OH for 24 h. The photoanode was rinsed with C$_2$H$_3$N and post baked for 10 min. Then, the counter electrode was coated with Pt with an active area of 0.67 cm^2 via spin coating method. Both of the electrodes were sandwiched and 0.5 M KI electrolyte were dropped on the gap. The overall device was sealed by silver paste.

2.5. Characterization

The surface morphologies of graphite, GO, and rGO were observed using field emission scanning electron microscopy (FESEM, FEI Quanta 200 FEG) with attachment of energy dispersive X-ray analysis (EDX), 5 kV. For surface morphologies of TiO$_2$, it was viewed under scanning electron microscopy TM3030 tabletop microscope at a working distance of approximately 2.0 mm at high vacuum mode with 5.0 kV. Besides, the rGO-TiO$_2$ nanocomposite was monitored under HITACHI UHR Cold-Emission FE-SEM SU 8000. The lattice of rGO-TiO$_2$ nanocomposite was examined under high-resolution transmission electron microscopy (HRTEM), JEM 2100F with an accelerating voltage of 200 kV. The topologies of the rGO-TiO$_2$ nanocomposite were measured using atomic force microscope controller—AFM5000II with 3D rotation. The purity phases of TiO$_2$, crystalline of rGO, and rGO-TiO$_2$ nanocomposite were determined using X-ray diffraction (XRD), D8 Advance X-ray

diffractometer-Bruker AXS, the spectra were measured from 10° to 70° with scanning rate of 0.033 deg/s under CuKα radiation (λ = 1.5418 Å). The structural characterization of rGO, TiO$_2$, and rGO-TiO$_2$ nanocomposite were recognized by the Raman analysis, Renishaw inVia microscope with applied HeCd laser source with λ = 514.0 nm at room temperature. Furthermore, its functional groups of rGO, TiO$_2$, and rGO-TiO$_2$ nanocomposite were identified under the Fourier transform infrared (FTIR) spectroscopy, Bruker-IFS 66/S along 500–4000 cm^{-1} wavelength by the KBr pellet method. The *J-V* curves of DSSCs were obtained from Autolab PGSTAT204 with solar irradiation (mercury xenon lamp) under 100 W input power.

3. Results and Discussion

3.1. Morphology

The FESEM images of graphite, graphene oxide (GO), and rGO are shown in Figure 4a–c, respectively. There are thick massive graphite flakes with nonuniform graphitic sheets distributed along the sample (Figure 4a). Figure 4b shows thin layers of GO after oxidation and exfoliation. On the other hand, Figure 4d shows the TiO$_2$ nanoparticles, which are sputtered on the surface of rGO to form the rGO-TiO$_2$ nanocomposite (Figure 4e) with average nanoparticles of ~30 nm (inserted in Figure 4e). Furthermore, the EDX results revealed that the atomic, at.%, content of carbon, C, element in the rGO-TiO$_2$ nanocomposite have been recorded at 37.29%, which is almost three times more than the titanium, Ti, element with 12.61%. However, the overall oxygen, O, remained the most contained element due to its contribution from the oxygenated group of graphene and also oxygen from TiO$_2$. The broad peak detected at 4.5 eV with high Ti content, is mainly due to the huge amount of Ti material sputtered and mixed along the rGO surface.
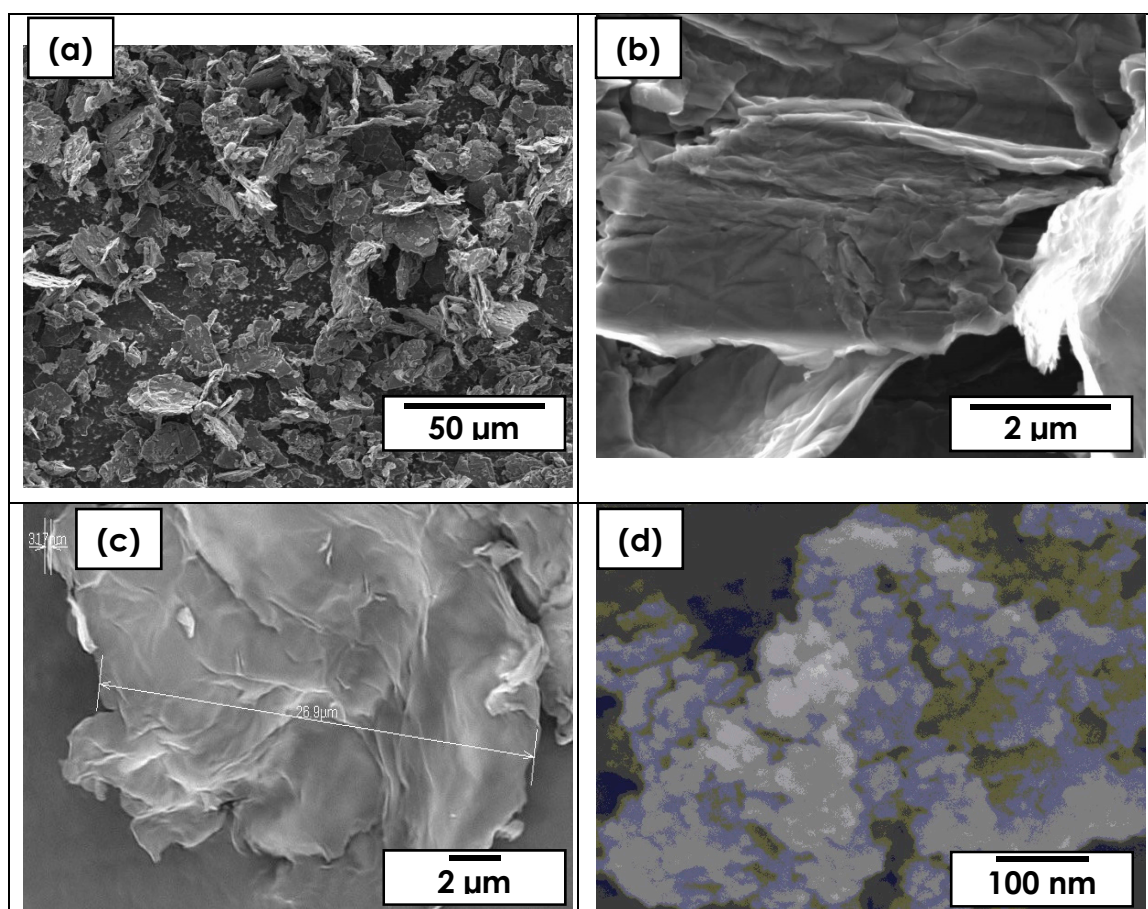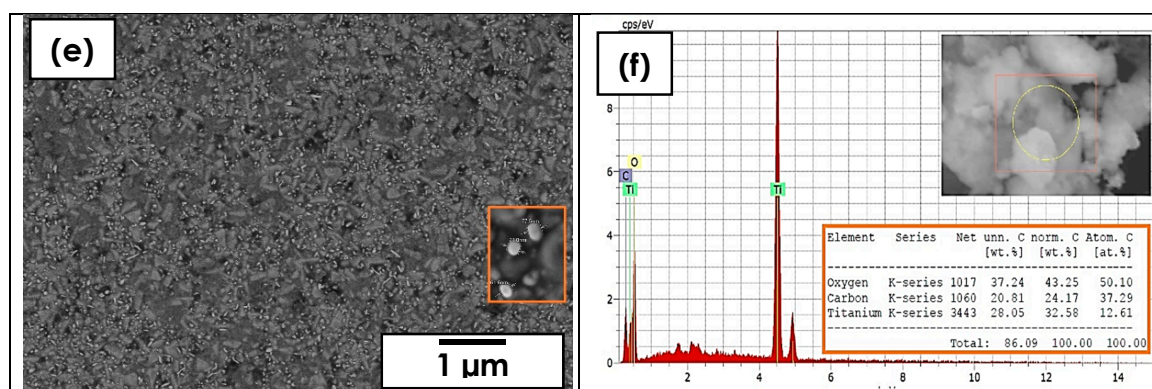

Figure 4. *Cont.*

Figure 4. FESEM images of (**a**) graphite, (**b**) GO, (**c**) rGO, (**d**) TiO$_2$, rGO-Ti ion implanted (**e**) at 120 °C, and (**f**) EDX data.

3.2. HRTEM

Further insight into the detailed microstructure of HRTEM and the typical image under 2 nm magnification determined that the TiO$_2$ is homogenously well anchored with rGO and formed rGO-TiO$_2$ nanocomposite as shown in Figure 5. Generally, the brighter color (0.336 nm) represented rGO nanomaterial; darker color (0.349 nm) those composed of TiO$_2$ nanoparticles, while grey color (0.399 nm) denoted the rGO-TiO$_2$ nanocomposite [33]. These phenomena were in agreement as Ti-O-C bonding, which was present and proven in Figure 8. The lattice fringes of the rGO (3.36°) and TiO$_2$ (3.49°) correspond to the rGO (002) plane and TiO$_2$ (101) plane, respectively [31].
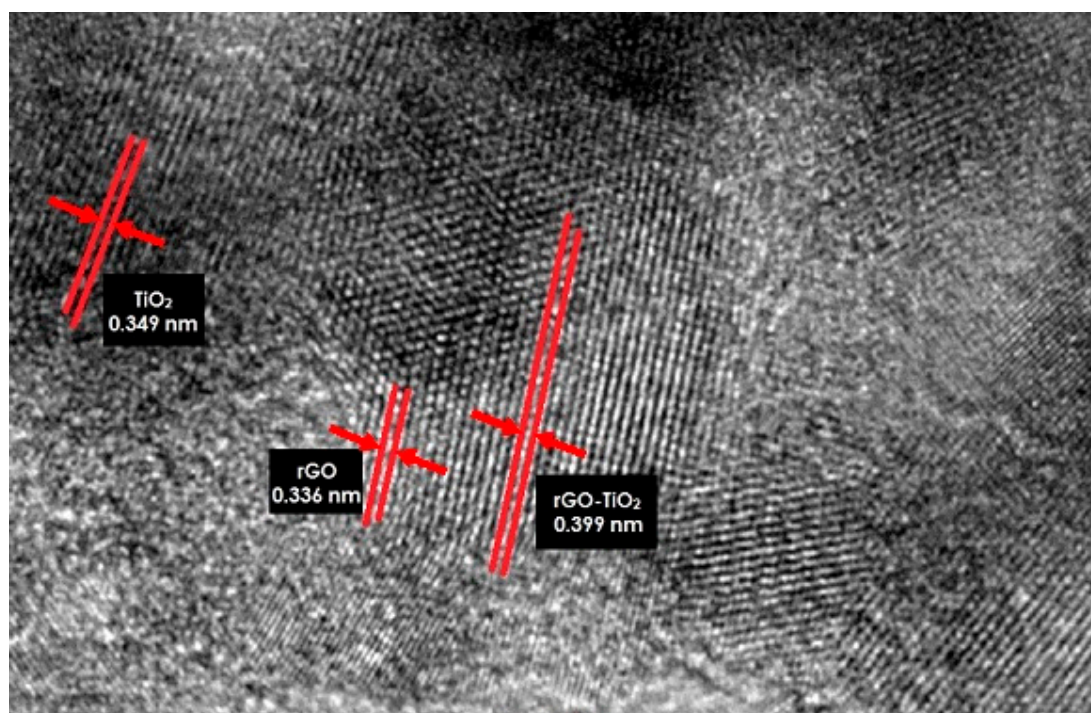

Figure 5. HRTEM image of 120 °C sputtered temperature of rGO-TiO$_2$ nanocomposite.

3.3. AFM

The topologies and cross-section of rGO-TiO$_2$ nanocomposite were analyzed by atomic force microscopy (AFM) as shown in Figure 6. Scanning areas for the surface were up to 300 nm × 300 nm whereas Figure 6a shows the 3D images with the highest depth of ~25 nm. In addition, the entire thickness with roughness of rGO-TiO$_2$ nanocomposite was ~75 nm, which the highest with brightest

color denoted as TiO_2. Besides, the 2D image was focused under 250 nm scan area for a better view on the surface roughness (refer Figure 6b). It is clearly shown that there are two different formation colors, whereby the bottom with darker color classified as TiO_2 was fully sputtered onto the rGO nanosheet and formed rGO-TiO_2 nanocomposite whereas the standalone brighter color represented sputtered TiO_2 that covered the top of the nanocomposite. Moreover, the cross-section of rGO-TiO_2 nanocomposite along Figure 6b revealed that the surface thickness was ~35 nm, which was in agreement with Figure 6a.
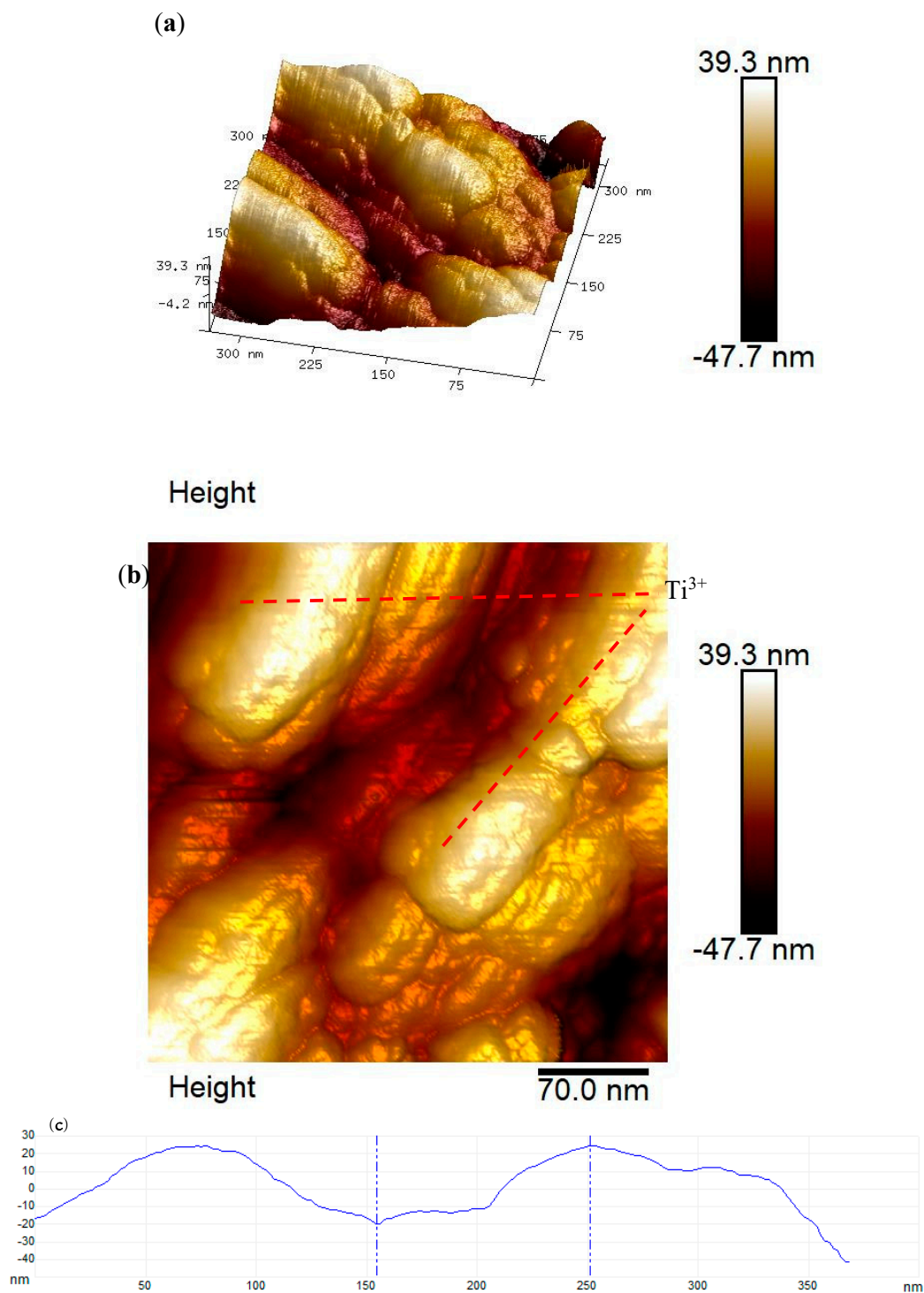

Figure 6. AFM images of 120 °C sputtered of rGO-TiO_2 nanocomposite for (**a**) 3D orientation, (**b**) particular focus area, and (**c**) cross-section data.

3.4. FTIR

The functional groups of graphene oxide (GO) and rGO were completely analyzed and identified as shown in Figure 7. Several intense peaks appeared in the GO sample, indicating oxygen containing groups that successfully formed from graphite after oxidation (Figure 7a). The absorption peaks including aromatic C-H deformation at 670 cm^{-1}, C-O stretching at 1052 cm^{-1}, phenolic C-OH stretching at 1200 cm^{-1}, C-OH at 1361 cm^{-1}, hydroxyl groups of molecular water and C=C at 1625 cm^{-1}, C=O stretching at 1729 cm^{-1}, and a broad peak assigned as O-H stretching vibrations of C-OH groups at 3400 cm^{-1} [31]. Definitely, the broad band of O-H stretching at 3400 cm^{-1} is significantly reduced and also the presence of C-O at 1052 cm^{-1} and C-OH at 1361 cm^{-1} in the rGO pattern. These phenomena clearly indicate that the GO has been reduced and the oxygenated group is eliminated [38].
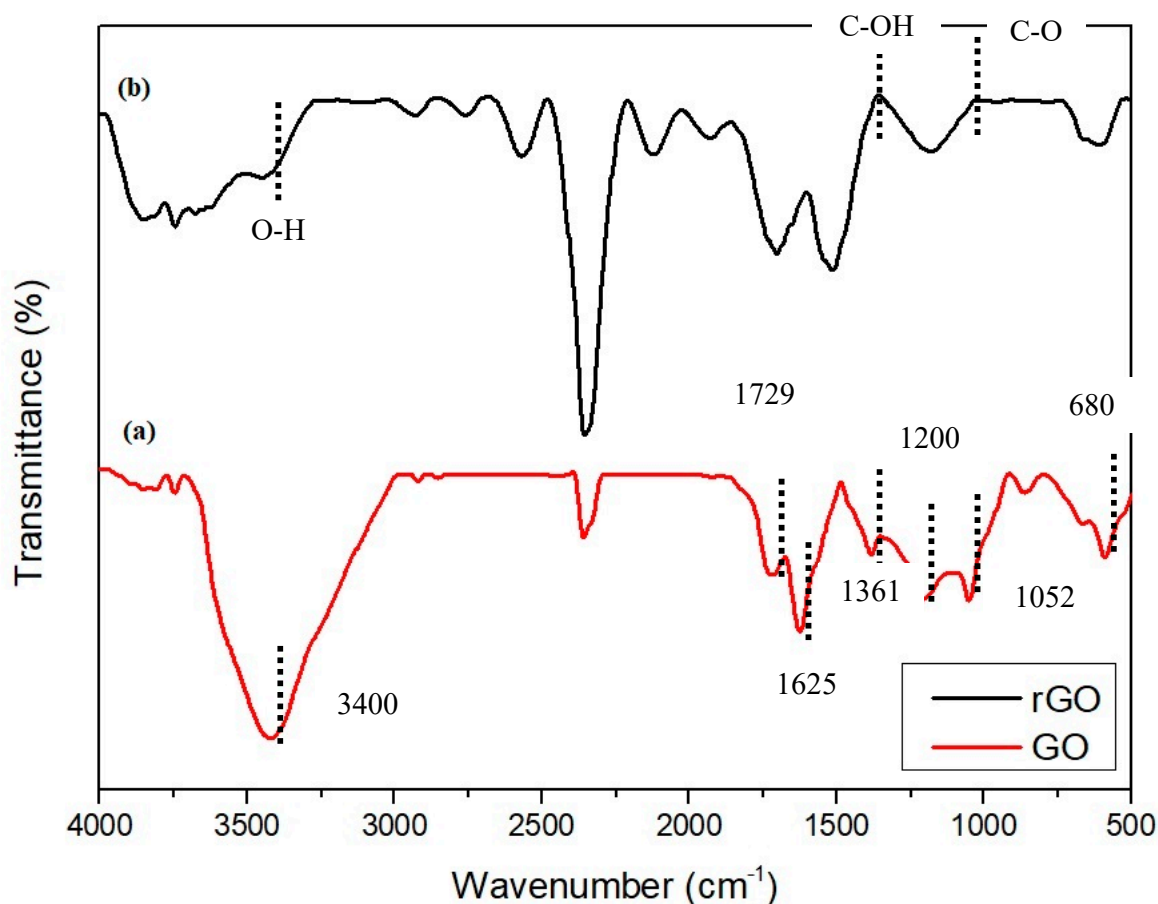

Figure 7. FTIR spectra of (**a**) GO and (**b**) rGO.

The FTIR transmission spectrum of rGO is placed in Figure 8 for further investigation between the TiO$_2$ and rGO-TiO$_2$ nanocomposite, which is formed via different sputtering temperatures. The FTIR spectrum of TiO$_2$ was also been identified and depicted the peaks as high purity TiO$_2$, which corresponded to TiO$_2$. From the TiO$_2$ spectrum, several peaks at 467 cm^{-1}, 1345 cm^{-1}, 1629 cm^{-1}, and 3396 cm^{-1} can be observed. To the best of our understanding, the broad peak in the range of 500–1000 cm^{-1} region is ascribed to the Ti-O and Ti-O-Ti bridging stretching modes while the peak is denoted as anatase titania [39]. In the rGO-TiO$_2$ samples, most of the rGO peaks did not appear in nanocomposite samples except 80 °C and 200 °C in the range between 1600–1750 cm^{-1}, which indicated high C=C content. Interestingly, the intense peak absorption appeared for each rGO-TiO$_2$ nanocomposite sample in the range of 550–900 cm^{-1} that was designated as Ti-O-C or Ti-O-Ti linkage bonds formed. This shows that these nanocomposite samples were well formed and established agreement for rGO-TiO$_2$ via sputtering method [40].
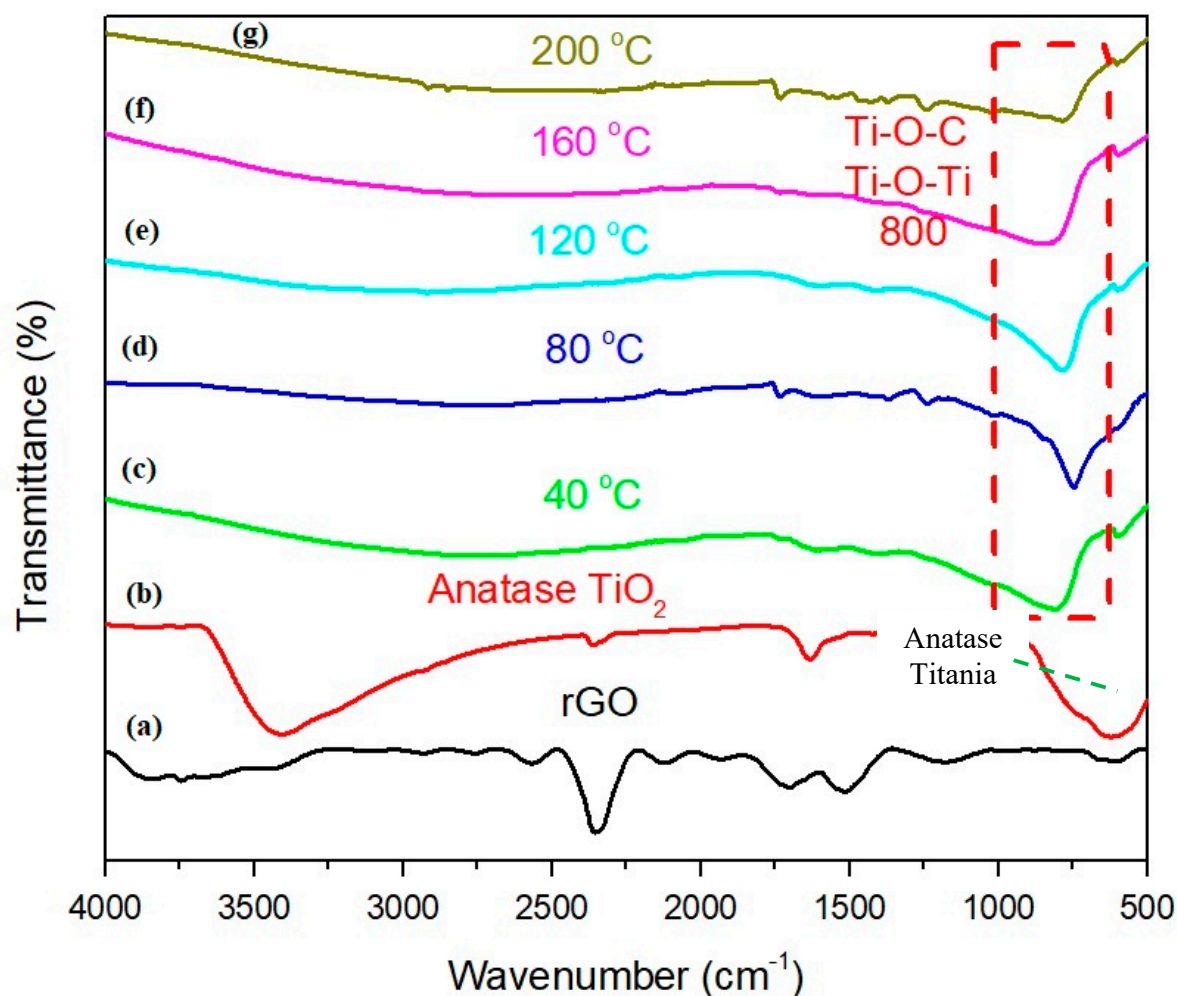
Figure 8. FTIR spectra of (**a**) rGO, (**b**) anatase TiO$_2$, and rGO sputtered TiO$_2$ via different temperature (**c**) 40 °C, (**d**) 80 °C, (**e**) 120 °C, (**f**) 160 °C, and (**g**) 200 °C.

3.5. XRD

The XRD pattern was utilized to analyze the crystallinity of introduced TiO$_2$ that sputtered onto the rGO nanostructure. Figure 9 shows the XRD spectra for synthesized rGO, TiO$_2$, and rGO-TiO$_2$ nanocomposites deposited at various sputtering temperatures. The XRD of rGO had a sharp peak presence at 25.2°, 43.8°, and 45.6° as shown in Figure 9a. These peaks correspond to (002), (001), and (001) diffraction planes while the 25.2° peak indicated that the reduction process from graphene oxide (GO) was successfully obtained [41,42]. Moreover, less intense peaks at 43.8° and 45.6° indicated highly disordered carbon material [32]. On the other hand, Figure 9b shows XRD patterns of high crystallinity TiO$_2$ as raw nanoparticle recorded in the range from 15° to 65°. The sharp Bragg peaks indicate that the highly crystalline TiO$_2$ nanomaterials are well-formed. The presence of the broad peaks and Bragg diffraction peaks indexed along 25.4°, 28.1°, 41.0°, and 54.6° with (101), (112), (211), and (204) orientations, respectively, corresponded to anatase phase TiO$_2$ (JCPDS card no: 21-1272) [43]. The XRD patterns from (c) to (g) were detected for rGO-TiO$_2$ nanocomposite in variations of sputtering temperature and well aligned along at 25.2°, which were in good agreement with the obtained unique properties along the (101) orientation.
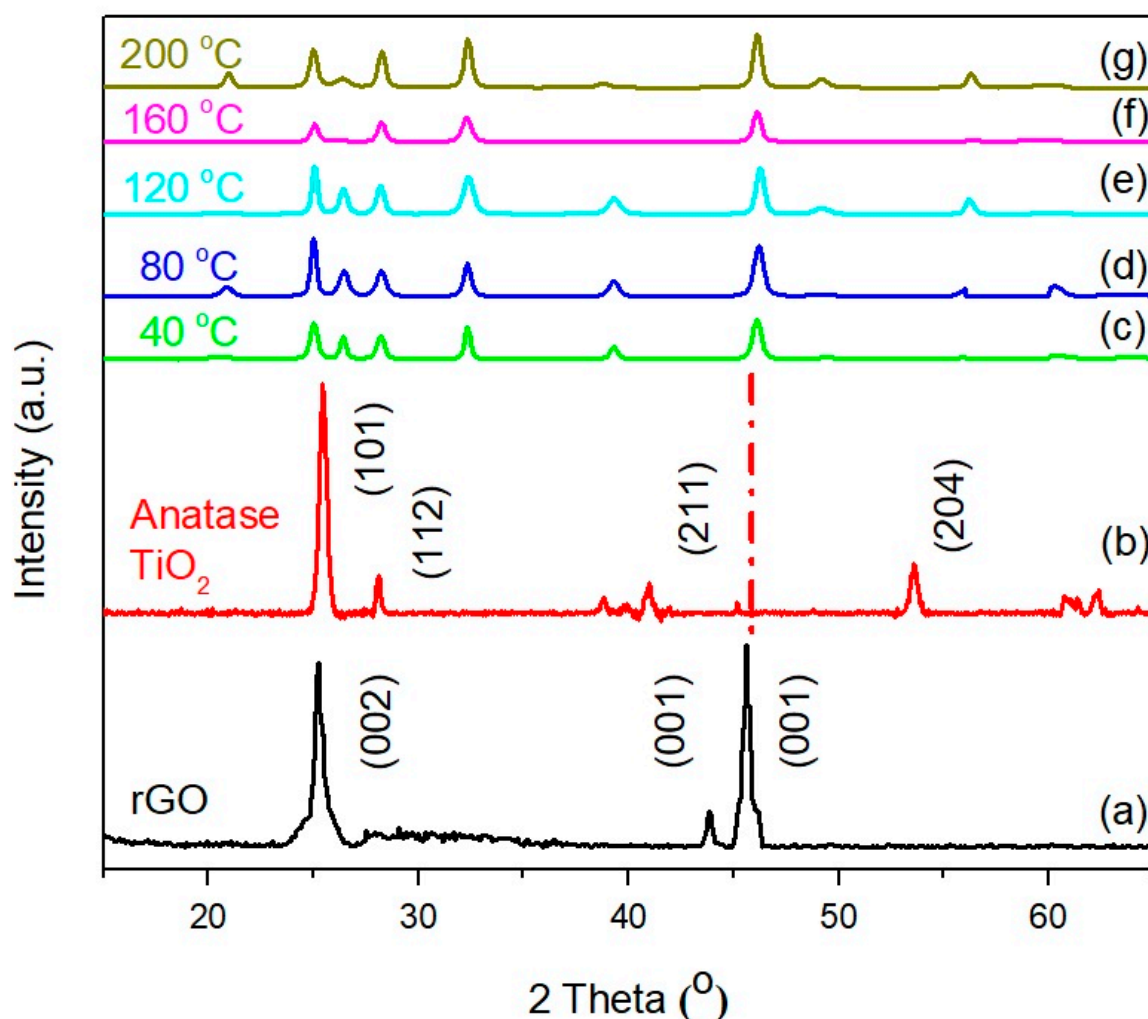
Figure 9. XRD patterns of (**a**) rGO, (**b**) anatase TiO$_2$, rGO-TiO$_2$ nanocomposite deposited at temperature of (**c**) 40 °C, (**d**) 80 °C, (**e**) 120 °C, (**f**) 160 °C, and (**g**) 200 °C.

3.6. Raman

　　The Raman spectra of rGO, anatase TiO$_2$, and rGO-TiO$_2$ nanocomposites deposited at temperatures of 40 °C, 80 °C, 120 °C, 160 °C, and 200 °C, respectively, are shown in Figure 10. The appearance of rGO peaks in the Raman spectrum of D band and G band at 1348.20 cm^{-1} and 1592.84 cm^{-1}, respectively, as analyzed in our previous work, confirmed successful reduction of GO to rGO [31,44]. Besides, the significance peaks for the sputtered TiO$_2$ have been identified as anatase phase TiO$_2$ due to the aligned Raman frequencies at 148.24 cm^{-1} (E$_{g1}$), 391.37 cm^{-1} (B$_{1g}$), 508.64 cm^{-1} (A$_{1g}$), and 629.65 cm^{-1} (E$_g$), which correspond to the literature [45]. Meanwhile, the Raman spectrum of rGO-TiO$_2$ nanocomposites with different sputtered temperatures have recognized entire material characteristics as every essential peak for particular anatase TiO$_2$ and rGO clearly appeared in the composite. Furthermore, the I$_D$/I$_G$ ratios of rGO and rGO-TiO$_2$ nanocomposites were calculated and displayed in Figure 10. The I$_D$/I$_G$ ratio could determine the defects of carbon nanomaterial based on the intensity of D band and G band. Among these rGO-TiO$_2$ nanocomposites, sputtered temperature condition at 80 °C was the highest defect credited to its I$_D$/I$_G$ ratio. In contrast, the sputtered temperature at 200 °C with lowest I$_D$/I$_G$ ratio indicated that the ideal sp^2 C-C network was well formed. Based on our understanding, D band-mode represented disordered structure of graphene material (sp^3-bonded) whereas G band arose from C-C bond stretching in graphitic material or known as more relevant to sp^2-bonded carbon atoms [46].
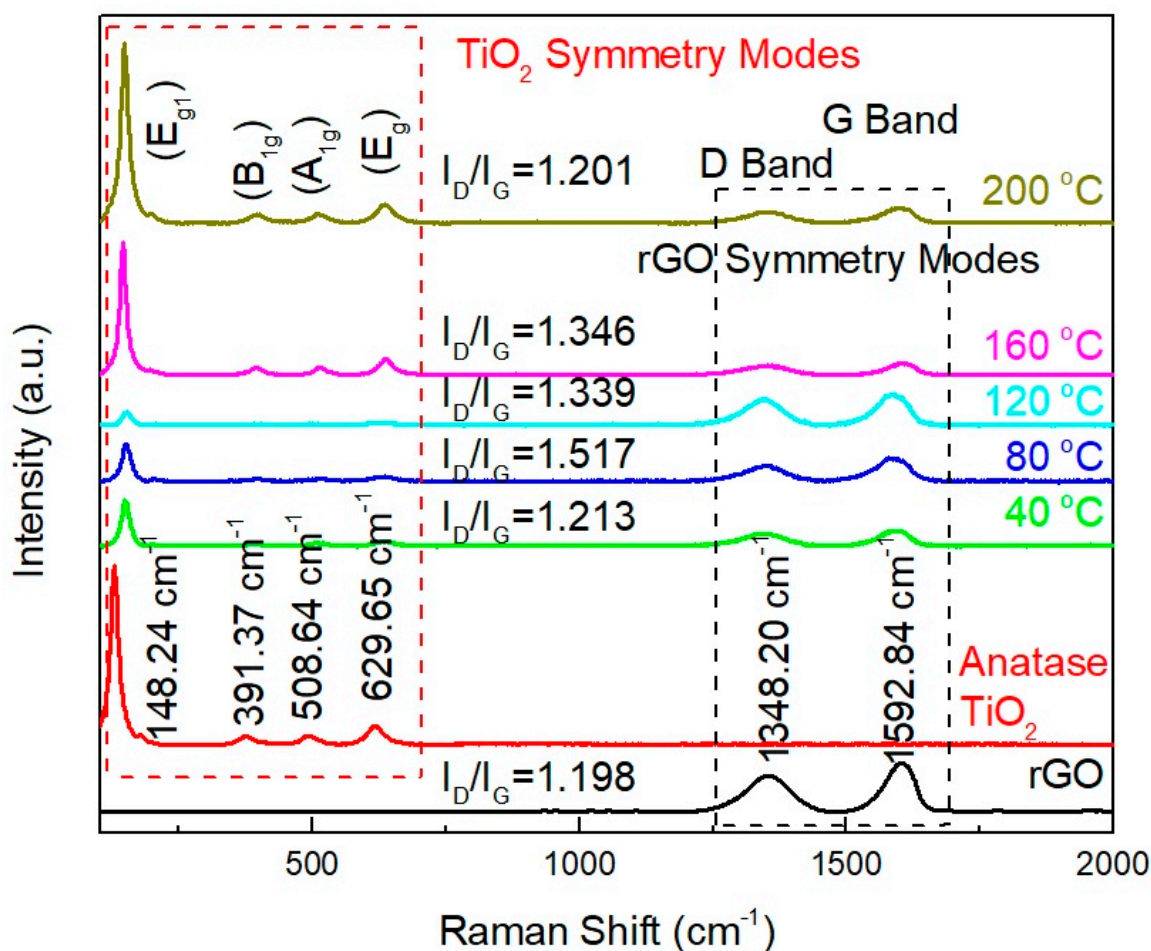
Figure 10. Raman spectra of rGO, anatase TiO_2, and rGO-TiO_2 nanocomposites based on different sputtered temperatures from 40 to 200 °C.

3.7. DSSCs

The DSSCs performance of sputtered raw TiO_2 and rGO-TiO_2 nanocomposite with different sputtering temperature onto rGO nanosheets were tabulated in Figure 11. The values of Table 2 are calculated based on the results in Figure 11 by reference from the equations below:

$$FF = \frac{V_{mp}J_{mp}}{J_{sc}V_{oc}} \tag{1}$$

$$\eta = \frac{J_{sc}V_{oc}FF}{P_{in}} \tag{2}$$

where *Jsc* = short circuit current; *Voc* = open circuit voltage; *Jmp* = maximum current; *Vmp* = maximum voltage; *FF* = fill factor; *Pin* = input power; and η = efficiency.

The PCE performance (η) of the DSSCs based on sputtering temperature studies of rGO-TiO_2 were determined accordingly by the details of photovoltaic characteristics such of DSSCs as short circuit current (*Jsc*), open circuit voltage (*Voc*), maximum power current (*Jmp*), maximum power voltage (*Vmp*), and fill factor (*FF*) (Table 2). It was revealed that 120 °C rGO-TiO_2 nanocomposites obtained an ideal PCE result of 7.27% with *Jsc* of 15.74 A/cm², *Voc* of 0.70 V, *Jmp* of 12.16 A/cm², *Vmp* of 0.60, and *FF* of 0.66. Among these rGO-TiO_2 nanocomposite samples, 120 °C also achieved the highest *Voc,* which indicated the shifting energy band of sputtered TiO_2 with effective transferring of the photoinjected electrons from excited electron into the conduction band [47]. Furthermore, this impact would definitely benefit the 120 °C rGO-TiO_2 nanocomposite with the efficient electron lifetime and obtained the highest value of *FF*.
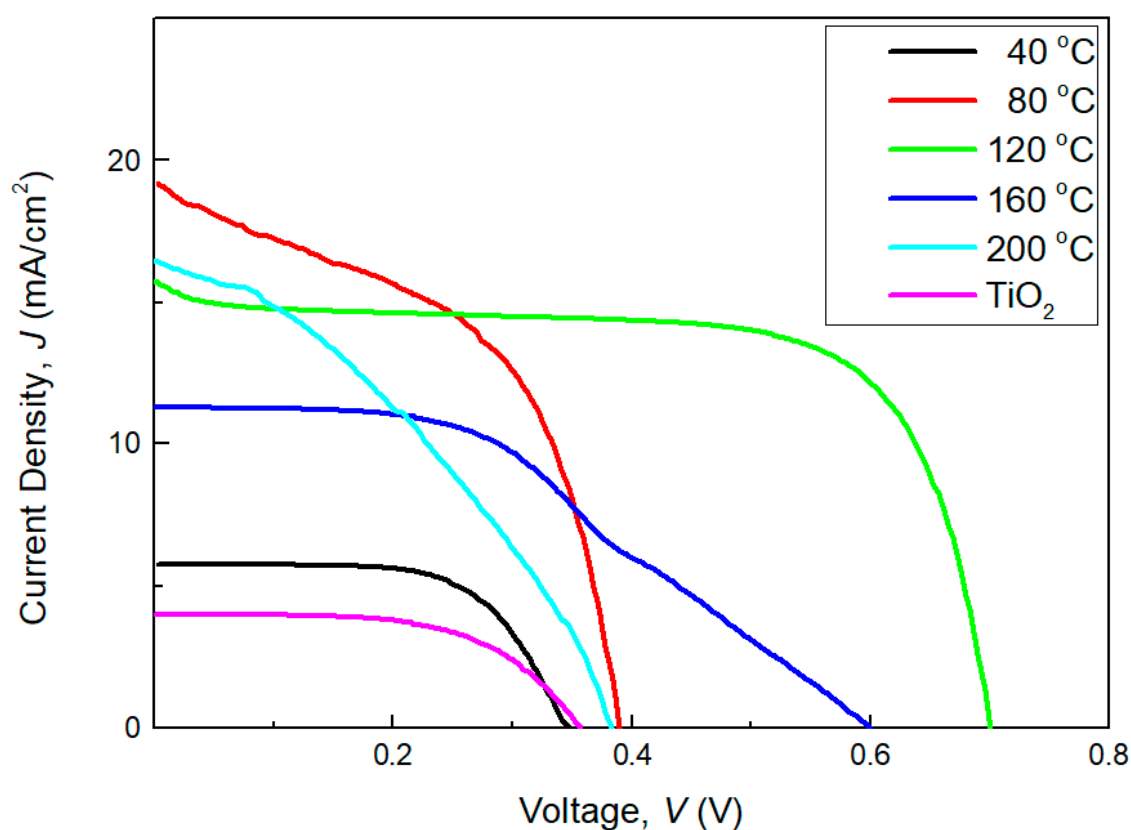
Figure 11. *J-V* curve of DSSCs based anatase TiO_2 and various sputtering temperatures of rGO-TiO_2 nanocomposite photoanodes film.

Table 2. Summary of photovoltaic characteristics of DSSCs via different sputtering temperatures of TiO_2.

Sputtering Temperature, °C	Short Circuit Current, *Jsc*	Open Circuit Current, *Voc*	Maximum Power Current, *Jmp*	Maximum Power Voltage, *Vmp*	Fill Factor, *FF*	Efficiency, *η*
TiO_2	3.98	0.36	2.82	0.28	0.55	0.79
40	5.75	0.35	5.07	0.25	0.63	1.27
80	19.18	0.39	12.58	0.30	0.50	3.74
120	15.74	0.70	12.16	0.60	0.66	7.27
160	11.31	0.60	9.69	0.30	0.43	2.92
200	16.46	0.38	14.85	0.10	0.24	1.50

From Table 2, a sputtered raw anatase TiO_2 was measured and attained the lowest PCE with 0.79% while 40 °C sputtering temperature of TiO_2 has the lowest PCE of 1.27% due to its small amounts of TiO_2 content reacts at photoanode element and difficult to absorb visible light from solar simulator [48]. The PCE is significantly increased from 40 °C with 1.27% to 80 °C and 120 °C with 3.74% and 7.27%, respectively. There was an estimate that improved by double according to the increases of sputtering temperature. In contrast, the PCE dramatically dropped from 7.27% to 2.92% (160 °C) and lastly to 1.50% (200 °C). This occurrence might be due to the excessive amount of TiO_2 which act as recombination centers that lead to high resistance of photo-induced charge carriers flow through the outer circuit [49].

4. Conclusions

This work discussed the effects of sputtering temperature of TiO_2 introduced onto rGO nanosheet and photoanode film for DSSCs PCE performance was accomplished. The sputtering route for rGO-TiO_2 nanocomposite formation is an impressive and effective approach. In this study, the rGO nanosheet was applied to facilitate photoinduced charge carrier electron transport while reducing electron-hole recombination pairs, resulting in better PCE performance of doped TiO_2. The uniform distribution

of TiO_2 was found at 120 °C sputtering temperature on the rGO nanosheet as demonstrated by FESEM images where the lattice of rGO, TiO_2, and rGO-TiO_2 nanocomposites were presented. Surface roughness of rGO-TiO_2 nanocomposite was measured at ~35 nm. Crystallinity of TiO_2 onto rGO nanosheets was analyzed and this confirmed that a mixture of TiO_2 anatase phase was sputtered. Both symmetry modes of rGO and anatase TiO_2 were presented on rGO-TiO_2 nanocomposite samples for various sputtering temperatures. The presence of Ti-O-C bonds was confirmed by FTIR spectra, associated with the oxygenated functional groups as shown in GO and rGO, respectively. It was found that 120 °C sputtering temperature eventually enhanced the overall mobility of electron transport to the outer circuit. The TiO_2 sputtered at 120 °C possessed the ideal PCE of 7.27%, five times better PCE than the 40 °C sputtering temperature. The results indicated that precise charge carrier loading concentration of TiO_2 is applied to achieve great absorptivity of dyes and charge separation, thus it improves the overall transportation properties. In contrast, the formation of rGO-TiO_2 nanocomposite at highest sputtering temperature with 200 °C acquired the lowest PCE performance of 1.50%, which is attributed to its excessive amounts of TiO_2 that penetrated and performed higher electron-hole pair recombination centers.

References

1. Khan, N.; Dilshad, S.; Khalid, R.; Kalair, A.R.; Abas, N. Review of energy storage and transportation of energy. *Energy Storage* **2019**, *1*, 1–49. [CrossRef]
2. Bais, A.F.; Lucas, A.F.; Bornman, J.F.; Williamson, C.E.; Sulzberger, B.; Austin, A.T.; Wilson, S.R.; Andrady, A.L.; Bernhard, G.; McKenzie, R.L.; et al. Environmental effects of ozone depletion, UV radiation and interactions with climate change: UNEP Environmental Effects Assessment Panel, update 2017. *Photochem. Photobiol. Sci.* **2018**, *17*, 127–179. [CrossRef] [PubMed]
3. Tefera, T.D.; Ali, S.F. Impacts of climate change on fish production and its implications on food security in developing countries. *Int. J. Food Nutr. Res.* **2019**, *3*, 1–13.
4. Islam, M.T.; Huda, N.; Abdullah, A.B.; Saidur, R. A comprehensive review of state-of-the-art concentrating solar power (CSP) technologies: Current status and research trends. *Renew. Sustain. Energy Rev.* **2018**, *91*, 987–1018. [CrossRef]
5. Munshi, A.H.; Sasidharan, N.; Pinkayan, S.; Barth, K.L.; Sampath, W.S.; Ongsakul, W. Thin-film CdTe photovoltaics–The technology for utility scale sustainable energy generation. *Sol. Energy* **2018**, *173*, 511–516. [CrossRef]
6. Shubbak, M.H. Advances in solar photovoltaics: Technology review and patent trends. *Renew. Sustain. Energy Rev.* **2019**, *115*, 109383. [CrossRef]
7. Green, M.A.; Dunlop, E.D.; Levi, D.H.; Hohl-Ebinger, J.; Yoshita, M.; Ho-Baillie, A.W.Y. Solar cell efficiency tables (version 54). *Prog. Photovolt. Res. Appl.* **2019**, *27*, 565–575. [CrossRef]
8. Khatri, I.; Matsuura, J.; Sugiyama, M.; Nakada, T. Effect of heat-bias soaking on cesium fluoride-treated CIGS thin film solar cells. *Prog. Photovolt. Res. Appl.* **2019**, *27*, 22–29. [CrossRef]
9. Fadaam, S.A.; Mustafa, M.H.; AlRazaK, A.H.A.; Shihab, A.A. Enhanced efficiency of CdTe Photovoltaic by thermal evaporation Vacuum. *Energy Procedia* **2019**, *157*, 635–643. [CrossRef]
10. Wen, X.; Chen, C.; Lu, S.; Li, K.; Kondrotas, R.; Zhao, Y.; Chen, W.; Gao, L.; Wang, C.; Zhang, J.; et al. Vapor transport deposition of antimony selenide thin film solar cells with 7.6% efficiency. *Nat. Commun.* **2018**, *9*, 1–10. [CrossRef]
11. Carella, A.; Borbone, F.; Centore, R. Research progress on photosensitizers for DSSC. *Front. Chem.* **2018**, *6*, 1–24. [CrossRef] [PubMed]

12. Basu, K. *Investigation of Heterostructure Photoanodes for Solar Energy Conversion*; Université du Québec, Institut National de la Recherche Scientifique: Quebec City, QC, Canada, 2018.

13. Liu, J.; Li, Y.; Arumugam, S.; Tudor, J.; Beeby, S. Investigation of low temperature processed titanium dioxide (TiO$_2$) films for printed dye sensitized solar cells (DSSCs) for large area flexible applications. *Mater. Today Proc.* **2018**, *5*, 13846–13854. [CrossRef]

14. Mbonyiryivuze, A.; Zongo, S.; Diallo, A.; Bertrand, S.; Minani, E.; Yadav, L.L.; Mwakikunga, B.W.; Dhlamini, S.M.; Maaza, M. Titanium Dioxide Nanoparticles Biosynthesis for Dye Sensitized Solar Cells Application. *Phys. Mater. Chem.* **2015**, *3*, 12–17.

15. Qian, R.; Zong, H.; Schneider, J.; Zhou, G.; Zhao, T.; Li, Y.; Yang, J.; Bahnemann, D.W.; Pan, J.H. Charge carrier trapping, recombination and transfer during TiO$_2$ photocatalysis: An overview. *Catal. Today* **2019**, *335*, 78–90. [CrossRef]

16. Ding, H.; Zhang, S.; Chen, J.T.; Hu, X.P.; Du, Z.F.; Qiu, Y.X.; Zhao, D.L. Reduction of graphene oxide at room temperature with vitamin C for RGO–TiO2 photoanodes in dye-sensitized solar cell. *Thin Solid Film.* **2015**, *584*, 29–36. [CrossRef]

17. Peiris, D.; Ekanayake, P.; Petra, M.I. Stacked rGO–TiO$_2$ photoanode via electrophoretic deposition for highly efficient dye-sensitized solar cells. *Org. Electron.* **2018**, *59*, 399–405. [CrossRef]

18. Kumar, K.A.; Subalakshmi, K.; Senthilselvan, J. Effect of co-sensitization in solar exfoliated TiO$_2$ functionalized rGO photoanode for dye-sensitized solar cell applications. *Mater. Sci. Semicond. Process.* **2019**, *96*, 104–115. [CrossRef]

19. Manikandan, V.; Palai, A.K.; Mohanty, S.; Nayak, S.K. Hydrothermally synthesized self-assembled multi-dimensional TiO$_2$/Graphene oxide composites with efficient charge transfer kinetics fabricated as novel photoanode for dye sensitized solar cell. *J. Alloys Compd.* **2019**, *793*, 400–409. [CrossRef]

20. Mahmood, T.; Aslam, M.; Naeem, A. Graphene/Metal oxide nanocomposite usage as photoanode in dye-sensitized and perovskite solar cells. In *Reconfigurable Materials*; IntechOpen: London, UK, 2020.

21. Wu, W.-T.; Yang, S.H.; Hsu, C.M.; Wu, W.T. Study of graphene nanoflake as counter electrode in dye sensitized solar cells. *Diam. Relat. Mater.* **2016**, *65*, 91–95. [CrossRef]

22. Tang, B.; Yu, H.; Peng, H.; Wang, Z.; Li, S.; Ma, T.; Huang, W. Graphene based photoanode for DSSCs with high performances. *RSC Adv.* **2018**, *8*, 29220–29227. [CrossRef]

23. Wei, W.; Wang, H.; Wang, C.; Luo, H. Advanced Nanomaterials and Nanotechnologies for Solar Energy. *Int. J. Photoenergy* **2019**, *2019*, 8437964. [CrossRef]

24. Kumar, V.; Bansal, A.; Gupta, R. Synthesis of rGO/TiO$_2$ Nanocomposite for the Efficient Photocatalytic Degradation of RhB Dye. In *Sustainable Engineering*; Springer: Berlin/Heidelberg, Germany, 2019; pp. 265–280.

25. Deshmukh, S.P.; Kale, D.P.; Kar, S.; Shisath, S.R.; Bhanvase, B.A.; Saharan, V.K.; Sonawane, S.H. Ultrasound assisted preparation of rGO/TiO$_2$ nanocomposite for effective photocatalytic degradation of methylene blue under sunlight. *Nano Struct. Nano Objects* **2020**, *21*, 100407. [CrossRef]

26. Khavar, A.H.C.; Moussavi, G.; Mahjoub, A.R. The preparation of TiO$_2$@ rGO nanocomposite efficiently activated with UVA/LED and H$_2$O$_2$ for high rate oxidation of acetaminophen: Catalyst characterization and acetaminophen degradation and mineralization. *Appl. Surf. Sci.* **2018**, *440*, 963–973. [CrossRef]

27. Leal, J.F.; Cruz, S.M.A.; Almeida, B.T.A.; Esteves, V.I.; Paula, A.; Marques, A.P.; Santos, E.B.H. TiO$_2$–rGO nanocomposite as an efficient catalyst to photodegrade formalin in aquaculture's waters, under solar light. *Environ. Sci. Water Res. Technol.* **2020**, *6*, 1018–1027. [CrossRef]

28. Nouri, E.; Mohammadi, M.R.; Lianos, P. Impact of preparation method of TiO$_2$-RGO nanocomposite photoanodes on the performance of dye-sensitized solar cells. *Electrochim. Acta* **2016**, *219*, 38–48. [CrossRef]

29. Lim, S.P.; Pandimumar, A.; Huang, N.M.; Lim, H.N. Reduced graphene oxide-titania nanocomposite-modified photoanode for efficient dye-sensitized solar cells. *Int. J. Energy Res.* **2015**, *39*, 812–824. [CrossRef]

30. Javed, H.M.A.; Qureshi, A.A.; Mustafa, M.S.; Que, W.; Mahr, M.S.; Shaheen, A.; Iqbal, J.; Saleem, S.; Jamshaid, M.; Mahmood, A. Advanced Ag/rGO/TiO$_2$ ternary nanocomposite based photoanode approaches to highly-efficient plasmonic dye-sensitized solar cells. *Opt. Commun.* **2019**, *453*, 124408. [CrossRef]

31. Low, F.W.; Lai, C.W.; Hamid, S.B.A. Surface modification of reduced graphene oxide film by Ti ion implantation technique for high dye-sensitized solar cells performance. *Ceram. Int.* **2017**, *43*, 625–633. [CrossRef]

32. Low, F.W.; Lai, C.W.; Hamid, S.B.A. Easy preparation of ultrathin reduced graphene oxide sheets at a high stirring speed. *Ceram. Int.* **2015**, *41*, 5798–5806. [CrossRef]

33. Low, F.W.; Lai, C.W.; Asim, N.; Akhtaruzzaman, M.; Alghoul, M.; Tiong, S.K.; Amin, N. An investigation on titanium doping in reduced graphene oxide by RF magnetron sputtering for dye-sensitized solar cells. *Sol. Energy* **2019**, *188*, 10–18. [CrossRef]

34. Lavin-Lopez, M.D.P.; Romero, A.; Garrido, J.; Sanchez-Silva, L.; Valverde, J.L. Influence of different improved hummers method modifications on the characteristics of graphite oxide in order to make a more easily scalable method. *Ind. Eng. Chem. Res.* **2016**, *55*, 12836–12847. [CrossRef]

35. Park, S.; An, J.; Potts, J.R.; Velamakanni, A.; Murali, S.; Ruoff, R.S. Hydrazine-reduction of graphite-and graphene oxide. *Carbon* **2011**, *49*, 3019–3023. [CrossRef]

36. Cho, C.-P.; Wu, H.-Y.; Lin, C.-C. Impacts of sputter-deposited platinum thickness on the performance of dye-sensitized solar cells. *Electrochim. Acta* **2013**, *107*, 488–493. [CrossRef]

37. Panepinto, A.; Michiels, M.; Durrschnabel, M.T.; Molina-Luna, L.; Bittencourt, C.; Cormier, P.-A.; Snyders, R. Synthesis of anatase (core)/rutile (shell) nanostructured TiO_2 thin films by magnetron sputtering methods for dye-sensitized solar cell applications. *ACS Appl. Energy Mater.* **2019**, *3*, 759–767. [CrossRef]

38. Tan, L.-L.; Ong, W.-J.; Chai, S.-P.; Mohamed, A.R. Reduced graphene oxide-TiO_2 nanocomposite as a promising visible-light-active photocatalyst for the conversion of carbon dioxide. *Nanoscale Res. Lett.* **2013**, *8*, 1–9. [CrossRef]

39. Rochman, R.A.; Wahyuningsih, S.; Ramelan, A.H.; Hanif, Q.A. Preparation of nitrogen and sulphur Co-doped reduced graphene oxide (rGO-NS) using N and S heteroatom of thiourea. In *IOP Conference Series: Materials Science and Engineering*; IOP Publishing: Bristol, UK, 2019.

40. Praveen, P.; Viruthagiri, G.; Mugundan, S.; Shanmugam, N. Structural, optical and morphological analyses of pristine titanium di-oxide nanoparticles–Synthesized via sol–gel route. *Spectrochim. Acta Part A Mol. Biomol. Spectrosc.* **2014**, *117*, 622–629. [CrossRef]

41. Gillespie, P.N.O.; Martsinovich, N. Origin of charge trapping in TiO_2/reduced graphene oxide photocatalytic composites: Insights from theory. *ACS Appl. Mater. Interfaces* **2019**, *11*, 31909–31922. [CrossRef]

42. Lazarte, J.P.L.; Dipasupil, R.C.; Pasco, G.Y.S.; Eusebio, R.C.P.; Orbecido, A.H.; Doong, R.; Bautista-Patacsil, L. Synthesis of reduced graphene oxide/titanium dioxide nanotubes (rGO/TNT) composites as an electrical double layer capacitor. *Nanomaterials* **2018**, *8*, 934. [CrossRef] [PubMed]

43. Yadav, H.M.; Kim, J.-S. Solvothermal synthesis of anatase TiO_2-graphene oxide nanocomposites and their photocatalytic performance. *J. Alloys Compd.* **2016**, *688*, 123–129. [CrossRef]

44. Low, F.W.; Lai, C.W.; Hamid, S.B.A. Study of reduced graphene oxide film incorporated of TiO_2 species for efficient visible light driven dye-sensitized solar cell. *J. Mater. Sci. Mater. Electron.* **2017**, *28*, 3819–3836. [CrossRef]

45. Castrejón-Sánchez, V.H.; Enrique, C.; Camacho-Lopez, M. Quantification of phase content in TiO_2 thin films by Raman spectroscopy. *Superf. Vacío* **2014**, *27*, 88–92.

46. Hodkiewicz, J. Characterizing carbon materials with Raman spectroscopy. *Thermo Sci. Appl. Note* **2010**, *51946*, 1–5.

47. Raja, R.; Govindaraj, M.; Antony, M.D.; Krishnan, K.; Velusamy, E.; Sambandam, A.; Subbaiah, M.; Rayar, V.W. Effect of TiO_2/reduced graphene oxide composite thin film as a blocking layer on the efficiency of dye-sensitized solar cells. *J. Solid State Electrochem.* **2017**, *21*, 891–903. [CrossRef]

48. Pichot, F.; Pitts, J.R.; Gregg, B.A. Low-temperature sintering of TiO_2 colloids: Application to flexible dye-sensitized solar cells. *Langmuir* **2000**, *16*, 5626–5630. [CrossRef]

49. Hasan, M.R.; Hamid, S.B.A.; Basirun, W.J.; Suhaimy, S.H.M.; Mat, A.N.C. A sol–gel derived, copper-doped, titanium dioxide–reduced graphene oxide nanocomposite electrode for the photoelectrocatalytic reduction of CO_2 to methanol and formic acid. *RSC Adv.* **2015**, *5*, 77803–77813. [CrossRef]

Sample Availability: Samples of the compounds are not available from the authors.